scribed from the geologic record, leading some workers to conclude that the Archean tectonic style was fundamentally different than that from younger times (*5*). The 50-km-long and 5-km-wide 2505 ± 2.2–Ma Dongwanzi ophiolite is the oldest recognized complete Archean ophiolite described from the geological record. The Dongwanzi ophiolite is identified on the basis of field data, consistent with the original definition and classical use of the term (*1*). As such, we interpret the ophiolite as representing a sample of oceanic crust and mantle, and we offer the following observations of regional relations that bear on the specific tectonic environment.

The Dongwanzi ophiolite forms a steeply northwest-dipping, northwest-facing sequence, in structural contact with underlying and overlying units. The ophiolite is located at the eastern edge of the Zunhua structural belt, interpreted as the Neoarchean suture between the eastern and western blocks of the North China craton (*9*). The eastern block has a Neoarchean magmatic arc built on its western margin, with the Zunhua belt in a structural position analogous to Phanerozoic accretionary wedges built on the edges of contemporaneous arcs. The Dongwanzi ophiolite and related rocks therefore likely represent fore-arc ophiolites formed in a suprasubduction zone setting or oceanic slivers accreted in the accretionary wedge and then thrust over the eastern block during collision of the eastern and western blocks of the North China craton.

The Dongwanzi ophiolite has a substantially thicker crustal section than that of younger ophiolite sequences (Fig. 2), suggesting that slightly higher mantle temperatures may have led to higher degrees of partial melting in the Archean mantle, forming thicker oceanic crust. The Dongwanzi ophiolite and similar Archean greenstone sequences provide important constraints on the thickness, thermal structure, chemistry, and petrogenesis of oceanic lithosphere in the Archean and offer rare insights for understanding heat loss mechanisms from early Earth.

References and Notes

1. Anonymous, *Geotimes* **17**, 24 (1972).
2. L. M. Parson, B. J. Murton, P. Browning, Eds., *Geol. Soc. Spec. Publ. London* **60**, 1 (1992).
3. A. Kontinen, *Precambrian Res.* **35**, 313 (1987).
4. D. J. Scott, H. Helmstaedt, M. J. Bickle, *Geology* **20**, 173 (1992).
5. M. J. Bickle, E. G. Nisbet, A. Martin, *J. Geol.* **102**, 121 (1994).
6. G. D. Harper, *Ophioliti* **10**, 297 (1985).
7. M. J. de Wit, R. A. Hart, R. J. Hart, *J. Afr. Earth Sci.* **6**, 681 (1987).
8. T. M. Kusky, A. Polat, *Tectonophysics* **305**, 43 (1999).
9. J. H. Li, X. L. Qian, X. N. Huang, S. W. Liu, *Acta Petrol. Sin.* **16**, 1 (2000).
10. J. H. Li, A. Kröner, X. L. Qian, P. O'Brien, *Acta Geol. Sin.* **274**, 246 (2000).
11. R. Y. Zhang, B. L. Cong, *Sci. Sin.* **25**, 37 (1982).
12. Q. C. Wang, S. Q. Zhang, in *Regional Geology of China* (Geological Publishing House, Beijing, 1995), pp. 173–180.
13. Supplemental Web material is available at www.sciencemag.org/cgi/content/full/292/5519/1142/DC1.
14. G. D. Harper, *Rev. Econ. Geol.* **8**, 53 (1999).
15. G. A. Davis *et al.*, in *The Tectonic Evolution of Asia*, A. Yin, T. M. Harrison, Eds. (Cambridge Univ. Press, New York, 1996), pp. 253–280.
16. We determined U-Pb zircon ages using methods developed by Krogh (*17, 18*), with modifications described in (*19*). Pb and U were loaded on single outgassed Re filaments and analyzed in a VG Sector-54 mass spectrometer by using a single-collector procedure with a Daly photomultiplier detector operating in ion-counting mode. In general, an ion beam between 0.5×10^{-14} and 1.5×10^{-13} Å was maintained for ^{206}Pb during data acquisition, and a beam between 0.5 and 1.5×10^{-13} Å was maintained for U. Average total procedural blanks of 2 pg of Pb and 0.2 pg of U were maintained during the period of analysis; total common-Pb concentrations for all analyses are reported in Web table 1 (*13*). Initial-Pb corrections used the Pb isotopic composition estimated in (*20*) at the indicated age of the rock. In nearly all cases, the uncertainty in the amount of and composition of common Pb calculated in this manner represents an insignificant contribution to the error of the calculated ages. Error propagation is similar to that developed in (*21*), and age errors are reported at 95% confidence limits. Analytical reproducibility at 1σ confidence levels of replicate samples confirms that the parameters used in data reduction (laboratory blank, fractionation, and Daly mass discrimination) and their errors have been evaluated correctly.
17. T. E. Krogh, *Geochim. Cosmochim. Acta* **37**, 485 (1973).
18. ———, *Geochim. Cosmochim. Acta* **46**, 637 (1982).
19. R. D. Tucker *et al.*, *Earth Planet. Sci. Lett.* **158**, 175 (1998).
20. J. S. Stacey, J. D. Kramers, *Earth Planet. Sci. Lett.* **26**, 207 (1975).
21. K. R. Ludwig, *Earth Planet. Sci. Lett.* **46**, 212 (1980).

22. Funding and support were provided by the Chinese National Natural Science Foundation, Academica Sinica, Peking University, St. Louis University, and Washington University. We thank X. Huang and Z. Zhang for assistance in the field and Z. X. Peng for assistance with the mass spectrometry and geochronology sample preparation.

30 January 2001; accepted 26 March 2001

Simultaneous Rupture Along Two Conjugate Planes of the Wharton Basin Earthquake

D. P. Robinson, C. Henry, S. Das,* J. H. Woodhouse

Analysis of broadband teleseismic data shows that the 18 June 2000 Wharton Basin earthquake, a moment magnitude 7.8 intraplate event in the region of diffuse deformation separating the Indian and Australian plates, consisted of two subevents that simultaneously ruptured two near-conjugate planes. This mode of rupture accommodates shortening by a mechanism different from that previously known elsewhere in the region. The larger subevent occurred on a fossil fracture zone, with a relatively high stress drop of about 20 megapascals, showing that large stresses can accumulate in regions of distributed deformation.

Plate motions in the Indian Ocean have been shown to be inconsistent with a rigid Indo-Australian plate (*1*). Additional diffuse boundaries splitting this plate into Indian, Australian, and Capricorn plates have been proposed (*2, 3*). The unexpectedly large earthquake under study here was located just west of the Investigator Fracture Zone (IFZ) (Fig. 1) in the Wharton Basin, near the southern edge of the region of deformation separating the Indian and Australian plates, and is far from all major plate boundaries. We use the term "intraplate" to refer to earthquakes that are not directly associated with the major plate boundaries. The earthquake occurred in a relatively old portion (~65 million years old) (*4*) of the oceanic crust. The general region is characterized by diffuse intraplate seismicity, mostly with earthquakes of magnitude <6, and no large earthquake has previously been recorded near the epicentral region. On the basis of the disturbance to the sedimentary cover obtained from sonar imagery combined with other available geophysical data, the region ~1000 km to the northwest of this earthquake has been inferred to be deforming predominantly along long N-S–trending left-lateral strike-slip faults (*5*). We recognize the long N-S features seen in the bathymetry between the Ninetyeast Ridge (90ER) and the IFZ, which includes the epicentral region, as fossil transform faults (*4, 5*). The compressional axes of earthquakes between longitudes of 90° and 100°E are consistently oriented NW-SE (Fig. 2), indicating that the intraplate stresses in this region are primarily inherited from the India-Asia collision. The long-wavelength (150 to 300 km) undulations seen in the gravity field, trending NE-SW in the Wharton Basin, have been proposed to indicate NW-SE shortening (*2*).

Most of the relocated aftershocks [see section 1 of Web material (*6*)] form a linear zone of ~110 km in length, trending ~345° (Fig. 3), suggesting that rupture occurred on a plane with

Department of Earth Sciences, University of Oxford, Parks Road, Oxford OX1 3PR, UK.

*To whom correspondence should be addressed. E-mail: das@earth.ox.ac.uk

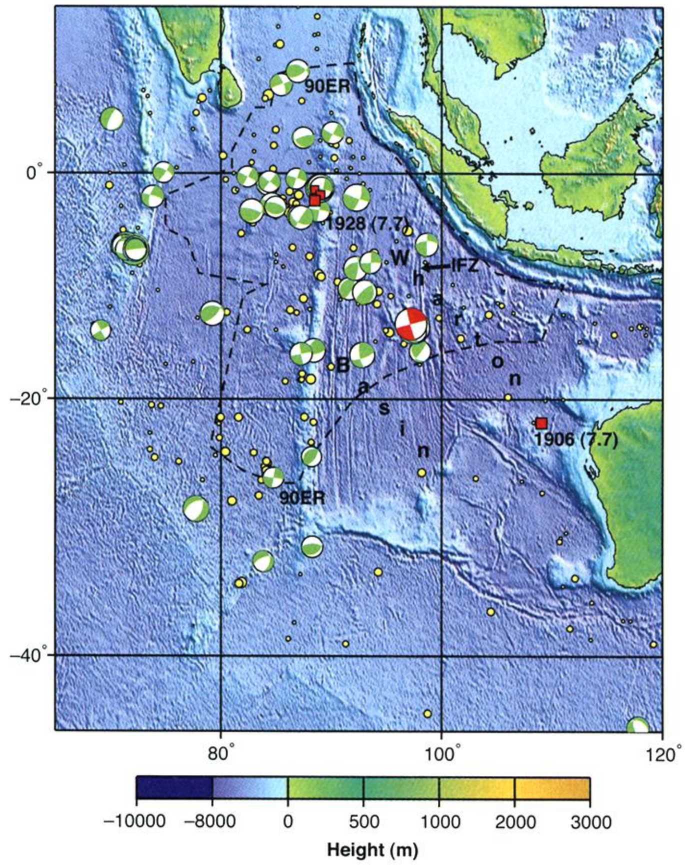

Fig. 1. Bathymetry (*12*) and all known intraplate oceanic seismicity before this earthquake from 1904 to August 1997 [reported by the International Seismological Center (ISC)] and since August 1997 (reported by the NEIC). The size of the yellow dots increases with earthquake magnitude. The main shock is indicated by the red CMT solution and was the largest known intraplate earthquake on the entire Indian Ocean part of the Indo-Australian plate. Available Harvard CMT solutions since 1977 (*15*) are shown in green. A large earthquake of magnitude 7.7 occurred in 1906 (22°S, 109°E), southeast of the Wharton Basin earthquake and close to the continental margin of Australia (*16*), and is shown by a red solid square. Another magnitude 7.7 earthquake (*16*) occurred in 1928 at 2.5°S, 88.5°E, near the 90ER, and is shown, along with its two large foreshocks, by red solid squares. The Investigator Fracture Zone is marked by "IFZ." The region of deformation inferred from the long-wavelength gravity data (*2*) is shown by the black dashed line.

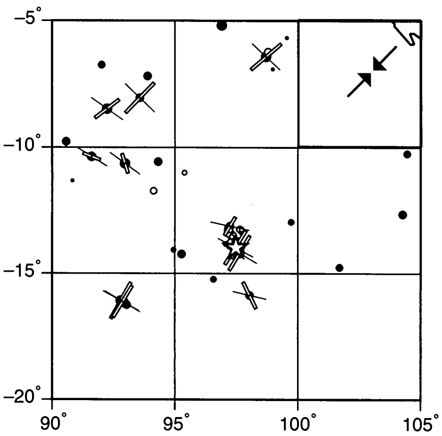

Fig. 2. Horizontal projections of stress axes (compressional axes, solid bars; tensional axes, open bars) in the region for intraplate earthquakes since 1977 (*15*), as well as those for this main shock (star) and its two large aftershocks. Epicenters before 31 August 1997 are from ISC (solid circles), and those since then are from NEIC (open circles). The arrows in the box at the top right indicate the direction of the compressional axes associated with the Sumatran subduction zone.

this general orientation. We recalculated the moment tensor by using mantle waves, which are the long period traces, typically with a duration of ~4 hours, containing the very long period fundamental mode Rayleigh and Love waves generated by the earthquake, together with their overtones. We find that the data can be equally well fit without the non–double-couple component obtained by the Harvard centroid moment tensor (CMT) solution (Fig. 3) [see section 2 of Web material (*6*)]. We also find that there exist two double-couple minima within a region of well-fitting solutions, shown in Fig. 3, A and B. However, neither the Harvard best double couple, nor either of these two double-couple mechanisms match the radiation pattern of the main *P*-wave pulse well. The mechanism inferred from this pulse (Fig. 3C) is the same as the nodal plane solution obtained from the polarity of the initial *P*-wave arrivals. We adopt this mechanism as the starting solution and invert 14 horizontal component *S* pulses (*SH*) to obtain the fault slip rate in space and time (*7*) [see section 3 of Web material (*6*)].

We cannot fit all of the seismograms at the same time by rupture on only one plane (*8*); in particular, no such solution was found that fits both station LSA (Lhasa, Tibet) to the north, having the largest *SH*-wave amplitude after reduction to a constant distance, and station PMG (Port Moresby, Papua New Guinea) to the east, with the second largest amplitude. Observed *P*- and *SH*-wave radiation patterns [Web fig. 1 (*6*)]

Table 1. Source parameters of the N-S– and E-W–trending rupture planes. Strike ϕ and dip δ are the angles that define the rupture plane, and the rake λ gives the direction of the earthquake slip motion, standard conventions being used (*17*). The length L of the fault is measured along the horizontal, and W is the fault width. The displacement across the faulted surface averaged over the fault area is the average slip $\bar{u}$. The seismic moment M_0 is obtained from the mantle wave spectra (*18*) and defined as $\mu L W \bar{u}$, where μ is the modulus of rigidity. M_w is the earthquake magnitude based on its seismic moment. The source duration t is the time during which there is motion on the fault surface. The average stress drop σ is given by $(2/\pi)\mu\bar{u}/W$. The rupture speed v is the average speed at which the rupture front propagates along the fault strike.

Parameter	Value	
	N-S plane	E-W plane
ϕ	165° ± 2°	75°
δ	87° ± 2°	82°
λ	−2° ± 4°	173°
M_0	5.8×10^{20} N·m	1.4×10^{20} N·m
M_w	7.8	7.4
L	50 ± 10 km N and 30 ± 10 km S of epicenter	50 km
W*	15 km	15 km
t	18 ± 3 s	~9 s
$\bar{u}$	8 m	~3 m
σ	~21 MPa	~8 MPa
v	3.1 ± 0.6 km s^{-1}	3 to 6 km s^{-1}

*Because of the very narrow fault width, we were unable to precisely obtain the extent of the rupture in depth. On the basis of many inversions, it is clear that no moment release occurred below 15 km, but we are not able to put error bars on this. Because $\bar{u}$ and σ are very sensitive to W, we also do not put error bars on them. Lower values of W would lead to larger values of $\bar{u}$ and σ.

strongly suggest that although rupture occurred with primarily northward directivity, some rupture must also have occurred on an E-W plane primarily toward the east. When we allow rupture on both nodal planes, we are able to fit the stations to the north and east far better, with the fit to all other stations being improved as well.

Our preferred solution [Table 1 and Web figs. 2 and 3 (*6*)] is the one with the minimum total moment, which is known to reduce spurious moment release (*9*). This seismic moment was found to be 7.2×10^{20} Nm (moment magnitude $M_w = 7.8$), which is consistent with the moments obtained from all CMT solutions. The earthquake consisted of two subevents (Fig. 4), with a total duration of ~27 s. For the first subevent, rupture occurred primarily on a nearly N-S–trending plane (strike 165°). The second subevent occurred with about a 15-s delay from the initiation time of the first subevent, starting ~45 km to the east of the N-S plane and propagating an additional ~50 km to the east on the near-conjugate plane (strike 75°). The best fitting N-S plane is well constrained, whereas the best E-W rupture plane is less so (*8*). No rupture west or immediately east of the main N-S fault is necessary to fit the data.

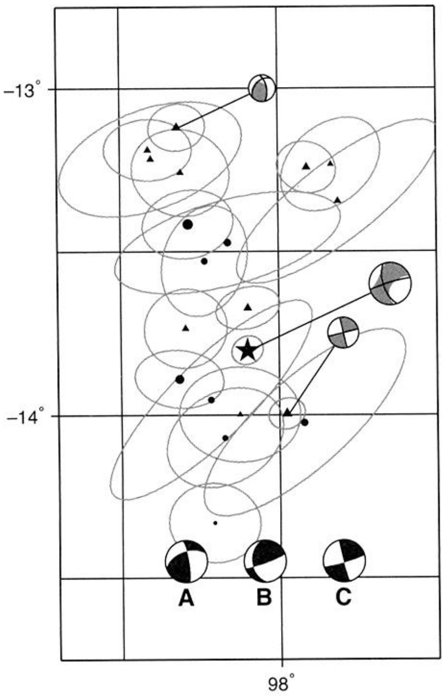

Fig. 3. Relocated aftershocks, together with 90% confidence error ellipses. The main shock is represented by the star. Circles indicate the first 7-hour aftershocks, and the rest are indicated by triangles. We plot only the 21 aftershocks that we were able to relocate. The Harvard CMT solutions (gray shaded, with the best double-couple mechanisms indicated by lines) are shown for the main shock and the two large aftershocks. Three additional CMT solutions are plotted at the bottom of the figure: (**A**) and (**B**) are the two best fitting pure double-couple solutions obtained by us, and (**C**) is the first motion solution that is the same as the solution inferred from the radiation pattern of the main *P*-wave pulse. These solutions are as follows: for (A), strike 350°, dip 80°, and rake 40°; for (B), strike 170°, dip 38°, and rake 12°. Both solutions have centroid locations close to −13.4°S, 97.3°E and their seismic moments M_0 are $\sim 7 \times 10^{20}$ N · m. The first motion solution for (C) is strike 165°, dip 87°, and rake 6°. The Harvard best double-couple mechanism is strike 161°, dip 63°, rake −5°, and $M_0 = 7.9 \times 10^{20}$ N · m.

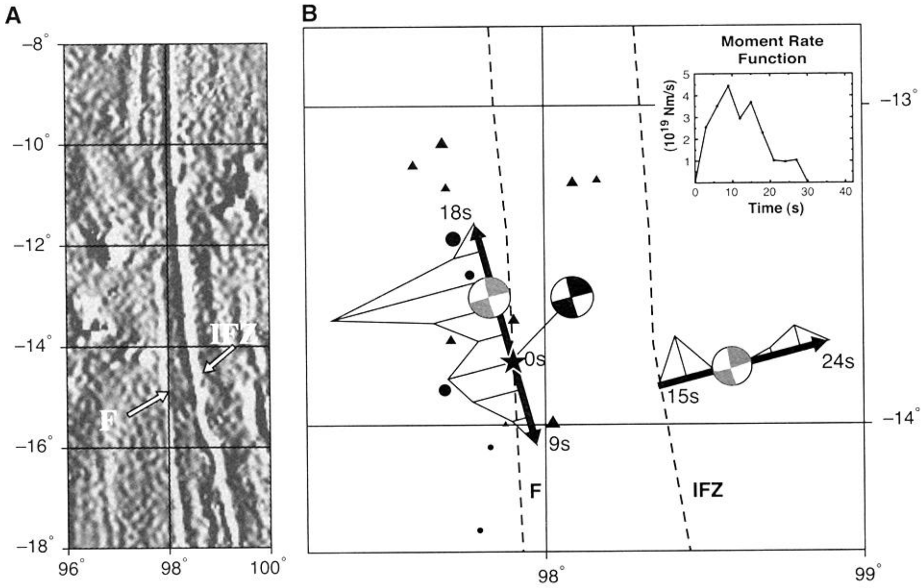

Fig. 4. (**A**) The bathymetry of the source region, showing the fracture zones IFZ and F. (**B**) A schematic showing the rupture propagation along the two near-conjugate fault planes. The black CMT solution is the sum of the individual rupture mechanisms (gray) for the N-S and E-W faults obtained in this study. Only aftershocks with 90% confidence ellipses of <30 km are plotted (symbols are the same as in Fig. 3). Graphs of the final moment distribution are superimposed, excluding regions with a moment of <10% of the maximum value on the N-S plane. IFZ and fracture F are indicated by dashed lines. The inset shows the moment rate function [see Web fig. 3 for details (*6*)].

We carry out an additional inversion and then reject the possibility that substantial moment could have occurred on the E-W fault immediately to the east of the N-S fault (*8*).

The rupture length on the N-S fault coincides with the 7-hour aftershock zone. The two largest aftershocks, with body wave magnitude $m_b = 5.4$ (20 min after the main shock) and $m_b = 5.6$ (2 days later), were located near the northern and southern terminations of the rupture, respectively. Aftershock activity essentially ceased after 4 days. The N-S rupture plane has few aftershocks for a typical subduction zone earthquake of this size, but both their low number and magnitude are consistent with those seen for other large oceanic strike-slip earthquakes (*9–11*). The E-W rupture zone had no aftershocks.

Of the long N-S fossil transform faults seen in the bathymetry of the Wharton Basin, the nearest one to the National Earthquake Information Center (NEIC) epicenter (50 km to the east, denoted as "F" in Fig. 4) lies close (~177°) to the strike of the near–N-S fault plane of this earthquake and is itself to the west of the IFZ. We consider it implausible that such a large earthquake could have occurred so close to, and parallel to, a major plane of weakness (fracture F) but on a causative fault without a bathymetric signature. We therefore suggest that the N-S rupture of the Wharton Basin earthquake actually occurred on fracture zone F and that the NEIC location results from the well-known difficulty of locating earthquakes in the middle of oceans far from seismic stations. Our inversions locate slip relative to the hypocenter, and thus, with this interpretation, the E-W rupture initiation is shifted onto the IFZ, a distance of ~45 km to the east of fracture F in this region (Fig. 4). The off-fault aftershocks to the northeast of the epicenter, two of which are reliably relocated (Fig. 3), lie close to the IFZ. The remainder of the aftershocks are either associated with the N-S rupture plane or lie to its west. The E-W rupture plane in this earthquake is consistent with the expected orientation of the ridge fabric. Closer examination of the predicted bathymetry (*12*) shows small elongated ridges northwest of this earthquake (not seen on the scale of Fig. 1) trending 75°, the strike of the second rupture plane.

Rupture on the long N-S–trending feature F is similar to the observation 1000 km farther northwest in the Wharton Basin (*5*), thus extending the region of known similar active deformation within the Indo-Australian plate. Motion on the conjugate E-W fault indicates that there is a component of NW-SE compressional deformation, in addition to shear on the N-S–trending faults. This is different from the region northwest of the hypocenter, as well as the 90ER, where some shortening occurs by thrust earthquakes (Fig. 1). Some of the other strike-slip earthquakes in the Wharton Basin having nodal plane directions similar to this earthquake may actually have ruptured on E-W nodal planes, a possibility that might otherwise be ignored because of the prominence of the N-S bathymetric features. Even though concurrent rupture on conjugate planes is rare, an example of rupture on conjugate planes in close proximity in time does exist. In November 1987, a $M_w = 7.2$ earthquake on a fault trending near–E-W in the Gulf of Alaska was followed less than 2 weeks later by a $M_w = 7.8$ earthquake on the conjugate N-S fault (*11*). These two earthquakes reactivated a fossil transform and a fossil ridge.

The spatial complexity of the rupture process of the Wharton Basin earthquake could not have been recognized by inspecting its moment rate function (Fig. 4), owing to the overlap of the two subevents in time [Web fig. 3 (*6*)]. Because of the previous lack of high-quality digital data with good azimuthal coverage of stations, particularly for earthquakes in remote parts of Earth, moment rate (source time) functions have been converted in some studies to spatial moment distributions on faults simply by adjusting them by a constant rupture velocity. This procedure makes the widespread implicit assumption that spatial complexity always manifests itself as complexity in the moment rate function, and complexity of plate boundaries in the past have been judged by looking at time functions of the source process of individual earthquakes. For this earthquake, such an assumption would have precluded identification of the eastward rupture and overestimated the length of the N-S one.

The occurrence of this large- and high-stress drop earthquake shows that large stresses can accumulate in an intraplate region of distributed deformation. The fact that there are no large earthquakes to the east of the IFZ suggests that the region of present-day active seismic deformation is smaller than the region of distributed deformation (Fig. 1) accumulated over millions of years and identified from the long-wavelength gravity field (*2*), a property also seen at the western side of the region. The region of deformation thus appears to be localizing with time onto a narrower N-S region.

References and Notes

1. C. DeMets, R. G. Gordon, D. F. Argus, S. Stein, *Geophys. J. Int.* **101**, 425 (1990).
2. J.-Y. Royer, R. G. Gordon, *Science* **277**, 1268 (1997).
3. R. G. Gordon, *Annu. Rev. Earth Planet. Sci.* **26**, 615 (1998).
4. R. D. Müller, W. R. Roest, J. Y. Royer, L. M. Gahagan, J. G. Sclater, *J. Geophys. Res.* **102**, 3211 (1997).
5. C. Deplus *et al.*, *Geology* **26**, 131 (1998).
6. Supplemental Web material is available at www.sciencemag.org/cgi/content/full/292/5519/1145/DC1.
7. The *P* waves for the largest aftershock are complex, in part because of water reverberations. *P* waves are sensitive to bathymetry, which varies in the source region because of the presence of seamounts and ridges. Hence, detailed modeling of the main shock *P* waves cannot be carried out reliably, although some properties of the rupture, such as directivity, are deduced by inspection of these waves. The *SH* waves, on the other hand, are unaffected by the water reverberations and have simpler waveforms, and hence we are able to reliably model these. The crustal structure CRUST 5.1 for this region (*13*) is consistent with the aftershock *SH* waves, and we used it in this study. We inverted *SH* waves to obtain the fault slip rate history and distribution [see section 3 of Web material (*6*)]. The spatial extent and duration of the parameterized source are taken to be larger than would be expected on the basis of an initial inspection of the aftershock zone and the preliminary moment rate function. This means that the true spatial extent and duration are determined as part of the solution, along with all other source parameters, such as rupture speed and average slip (as listed in Table 1), and not assigned a priori. For this earthquake, we used a 300-km N-S fault centered on the epicenter and a 200-km E-W fault centered on the N-S fault. We divided these faults into 10-km cells along strike. Along the dip direction, we have one cell extending throughout the crust (7 km thick) and a second cell below the crust extending to a depth of 15 km. We used 3-s time steps, and every cell is allowed to slip at every time step, except when this would be in advance of a 6 km s^{-1} wavefront emitted from the hypocenter. We imposed the physically motivated constraint that the moment rate must be positive in all cells at all time steps, which is known to be essential to obtain a stable solution (*14*).
8. We first carried out inversions to obtain the best single rupture plane. We tried many possible faults [see section 4 of Web material (*6*)] close to each of the N-S and E-W nodal planes. No prior assumptions about directivity were made for these inversions. In each of ~75 such inversions, we failed to fit all of the seismograms. In order to fit the stations to the north and east, rupture must have occurred on both nodal planes. Thus, in a series of ~20 further inversions, rupture is simultaneously permitted on both nodal planes, still without any prior assumptions about directivity. The best fitting E-W plane is slightly different from the conjugate plane of the N-S rupture plane, with the exact conjugate plane fitting the data less well. Sixteen further inversions were carried out to investigate the range of moments on each fault plane and the possible locations of the E-W rupture consistent with the data. We found that placing the E-W fault plane south of the epicenter provides a slightly better fit to the data than placing it to pass through the epicenter. Because the E-W rupture initiated while motion was still continuing on the N-S rupture plane and because it has a smaller M_w, its parameters cannot be as well resolved as those for the N-S rupture, and hence we cannot provide their error bars in Table 1. The principal features of the preferred solution that we discuss and interpret are also present in all of our other inversions and can thus be regarded as robust [see section 4 of Web material (*6*)]. To test if any moment could have been released immediately east of the main N-S fault, we searched for the solution with maximum moment released in this region. We found for this case that the total moment on the E-W fault is reduced and does not exceed 40% of its previous value, with all the moment being shifted into this region. However, the resulting deterioration of the fit of the stations to the east indicates that this solution does not possess sufficient directivity to the east, and hence we reject the possibility that substantial moment could have occurred on the E-W fault immediately to the east of the N-S fault.
9. C. Henry, S. Das, J. H. Woodhouse, *J. Geophys. Res.* **105**, 16097 (2000).
10. S. Das, *Geophys. J. Int.* **115**, 778 (1993).
11. G. Pegler, S. Das, *Tectonophysics* **257**, 111 (1996).
12. W. H. F. Smith, D. T. Sandwell, *Science* **277**, 1956 (1997).
13. W. D. Mooney, G. Laske, T. G. Masters, *J. Geophys. Res.* **103**, 727 (1998).
14. S. Das, B. V. Kostrov, *J. Geophys. Res.* **95**, 6899 (1990); S. Das, B. V. Kostrov, *Phys. Earth Planet. Inter.* **85**, 293 (1994).
15. A. M. Dziewonski *et al.*, *Phys. Earth Planet. Inter.* **33–121** (1983–2000).
16. B. Gutenberg, C. F. Richter, *Seismicity of the Earth and Associated Phenomena* (Princeton Univ. Press, Princeton, NJ, 1954).
17. K. Aki, P. G. Richards, *Quantitative Seismology: Theory and Methods* (Freeman, New York, 1980).
18. A. M. Dziewonski, J. H. Woodhouse, in *Proceedings of the International School of Physics "Enrico Fermi," LXXXV, Varenna, 29 June to 9 July, 1982, Italian Physical Society*, H. Kanamori, E. Boschi, Eds. (North-Holland, Amsterdam, 1983), pp. 45–137; *J. Geophys. Res.* **88**, 3247 (1983).
19. D.P.R. is supported by the Salford (U.K.) Local Education Authority and the Oppenheimer Fund of Worcester College, Oxford; C.H. is supported by U.K. Natural Environment Research Council (NERC) studentship GT04/97/ES/217 and a Schlumberger Cooperative Awards in Sciences of the Environment grant. Computations were carried out under NERC grant GR9/03960, and the Oxford seismological data facility was supported by NERC grant GR11534.

29 January 2001; accepted 23 March 2001

Sudden Productivity Collapse Associated with the Triassic-Jurassic Boundary Mass Extinction

P. D. Ward,[1]* J. W. Haggart,[2] E. S. Carter,[3] D. Wilbur,[4] H. W. Tipper,[2] T. Evans[1]

The end-Triassic mass extinction is one of the five most catastrophic in Phanerozoic Earth history. Here we report carbon isotope evidence of a pronounced productivity collapse at the boundary, coincident with a sudden extinction among marine plankton, from stratigraphic sections on the Queen Charlotte Islands, British Columbia, Canada. This signal is similar to (though smaller than) the carbon isotope excursions associated with the Permian-Triassic and Cretaceous-Tertiary events.

The Triassic-Jurassic (T-J) boundary mass extinction, one of the five most severe in Phanerozoic history, led to the demise of as many as 80% of all living species (*1–3*). Unanswered questions about the extinction concern its duration, its severity, and whether it affected global productivity. The extinction in marine strata has recently been dated at 199.6 ± 0.3 million years ago (Ma) by means of high-resolution U-Pb zircon geochronometry (*4*), but it is unknown whether the extinctions were synchronous on land and in the sea, because this date seems slightly later than the extinction dated on land (*5*). It has been suggested that the T-J extinction, unlike the Permian-Triassic (P-T) and Cretaceous-Tertiary (K-T) events, did not affect the carbon cycle long enough to cause a clear perturbation in δ^{13} organic carbon ($\delta^{13}C_{org}$) (*6*).

[1]Department of Earth and Space Sciences, University of Washington, Seattle, WA 98195, USA. [2]Geological Survey of Canada, Vancouver, British Columbia V6B 5J3, Canada. [3]Department of Geology, Portland State University, Portland, OR 97207, USA. [4]Department of Oceanography, University of Washington, Seattle, WA 98195, USA.

*To whom correspondence should be addressed.